https://doi.org/10.1016/j.cmpb.2020.105828

Extended Kalman Filter Nonlinear Finite Element Method for Nonlinear Soft Tissue Deformation

Hujin Xie[1], Jialu Song[1], Yongmin Zhong[1], Jiankun Li[1], Chengfan Gu[1], Kup-Sze Choi[2]

[1]School of Engineering, RMIT University, Australia
[2]School of Nursing, The Hong Kong Polytechnic University

ABSTRACT

Background and Objective: Soft tissue modelling is crucial to surgery simulation. This paper introduces an innovative approach to realistic simulation of nonlinear deformation behaviours of biological soft tissues in real time.

Methods: This approach combines the traditional nonlinear finite-element method (NFEM) and nonlinear Kalman filtering to address both physical fidelity and real-time performance for soft tissue modelling. It defines tissue mechanical deformation as a nonlinear filtering process for dynamic estimation of nonlinear deformation behaviours of biological tissues. Tissue mechanical deformation is discretized in space using NFEM in accordance with nonlinear elastic theory and in time using the central difference scheme to establish the nonlinear state-space models for dynamic filtering.

Results: An extended Kalman filter is established to dynamically estimate nonlinear mechanical deformation of biological tissues. Interactive deformation of biological soft tissues with haptic feedback is accomplished as well for surgery simulation.

Conclusions: The proposed approach conquers the NFEM limitation of step computation but without trading off the modelling accuracy. It not only has a similar level of accuracy as NFEM, but also meets the real-time requirement for soft tissue modelling.

Keywords: Soft tissue modelling, nonlinear FEM, extended Kalman filter, and real-time performance.

1. Introduction

Modelling of biological tissue deformation is important to surgery simulation, which requires the soft tissue model to exhibit both physical fidelity and real-time performance under a mechanical load. Nevertheless, given the conflict of both requirements, modelling of mechanical deformation of biological tissues is a challenging research issue [1, 2].

Biological soft tissue modelling has received a great deal of attention in the past decades. The early work focused on geometrically based modelling to employ various geometrical tools such as spline surfaces [3] for tissue mechanical deformation. In spite of efficient computations, the approach of geometrically based modelling lacks the physical realism for tissue mechanical deformation, since the mechanical attributes of soft tissues are not considered.

In the recent decade, research efforts have focused on physically based modelling to handle the physical realism of tissue mechanical deformation by incorporating mechanical properties of soft tissues and physically dynamic motions in the modelling process. The mass spring deformation is a traditional method for tissue mechanical deformation, where the tissue model is discretized into mass nodes interconnected via a network of springs. This method has a simple implementation and is capable of real-time modelling. However, its modelling accuracy is poor. The ChainMail model [4, 5] is an alternative to MSM. It replaces the spring between mass nodes with the bounding region of a chain element to control element movement, where the movement of a chain element is occurred when this element is located out of its bounding region imposed by its neighbouring elements. In spite of its simple mechanism of element movement, the ChainMail model requires the selection of geometric limits to appropriately define the bounding region for deformation [6, 7]. Position-based dynamics is also an approach to dynamic deformation [8]. However, since the position-based dynamic process is fundamentally based on geometry, this method has limited accuracy. To address this issue, various physical constraints such as potential energy reduction [9] and energy balance [10] are incorporated in position-based dynamics, while only leading to a certain level of visual plausibility for tissue mechanical deformation.

Modelling on the basis of continuum mechanics is an effective solution to address the accuracy for tissue mechanical deformation. The representative instance is the finite element method (FEM) [6], where rigorous continuum constitutive laws are employed to accurately account for mechanical deformation of biological tissues [11, 12]. However, FEM involves an expensive computational load [13, 14]. Accordingly, the current studies on using FEM for soft tissue deformation are mainly dominated by linear elasticity which permits reduced runtime computation since the global stiffness matrix is constant [13]. However, due to the assumption of small deformation within a short time period, linear elasticity cannot account for nonlinear and large-range deformation behaviours of soft tissues. To overcome this limitation, various techniques such as the co-rotational FEM to warp the global stiffness matrix via node rotations [15], the replacement of linear strains with quadric strains, and the incorporation of nonlinear items into linear material parameters [16], were studied to add nonlinearity into a linear FEM model. However, suffering from the limitation of linear elasticity, these improvements only exhibit geometrical rather than material nonlinearity. Although the nonlinear FEM (NFEM) can handle nonlinear material properties, due to the complexity in formulating and calculating nonlinear elasticity, it is extremely complicated to attain the dynamic performance for tissue mechanical deformation [13, 17].

Studies were devoted to improving the FEM computational performance. Matrix condensation simplifies FEM computations from 3D volume to 3D boundary surface, while leading to degraded modelling accuracy [18]. The pre-computation technique computes steady-state elementary deformations before the iterative procedure to reduce the FEM runtime cost [19]. However, it involves complex computations, which are time-consuming. The GPU (Graphics Processing Unit) acceleration improves the computational performance of FEM via GPU [20, 21]. Nevertheless, this technique relies on physical hardware. Adaptive remeshing reduces the FEM computational time using an automatic procedure of mesh refinement [22]. In addition to the additional work caused by the re-meshing process, the improvement of computational performance is achieved at the cost of decreased accuracy. The technique of model order reduction [23-25] reduces the FEM runtime cost by approximating the FEM solution with a set of global basis functions. However, the modelling accuracy is degraded due to the error involved in the numerical approximation. Machine learning is also a technique to facilitate the FEM computations [26]. However, this technique involves a learning process whose accuracy depends on a large amount of samples, leading to an expensive computational cost.

The tensor-mass model simplifies the complex FEM formulation by lumping masses and forces at node level for deformation computations [27]. In spite of reduced complexity in computation, this simplification method causes a significant degradation of accuracy. The strain-limiting FEM reduces the complexity of FEM computations by incorporating constraints in FEM to calculate the strain limits. However, this method requires constraint definition and solving to appropriately define the strain limits for the physical realism. The total Lagrangian formulation combines the lumped-mass and explicit time integration techniques to reduce the runtime computations of FEM [28, 29]. However, it has to recompute 3D partial derivatives at each time step, increasing the computational load. The meshless method [30] simplifies the complexity of FEM computations, since it constructs the basis function without the object mesh. However, it has to identify the node neighbourhood at each time step, resulting in additional computational burdens. It also lacks theoretical analysis on error boundness for numerical integration and is difficult to cope with sparsely sampled regions [31]. Generally, with the current methods, the FEM runtime cost is improved by sacrificing the modelling accuracy [28, 32]. The detailed literature survey on FEM-based soft tissue modelling can be found in [13, 28, 33].

Kalman filtering represents a classical method to estimate the dynamic state of a system from feedback measurement and has been applied in various biomedical applications [34-37]. Due to its elegant recursive characteristics, this method has the advantage of computational efficiency for achieving optimal estimations. However, Kalman filtering only conducts system state estimation in the temporal domain. Thus, combining Kalman filtering with FEM offers a resolution for system state estimation in both space and time. Currently, there are few studies on combination of Kalman filtering with FEM for dynamic modelling of tissue mechanical deformation. The authors recently studied a method by combination of Kalman filtering and FEM for online deformation prediction [38]. This method is based on the standard Kalman filter and linear FEM, as the standard Kalman filter is linear and can be used with linear systems only. However, due to the limitation of linear elasticity, it can only model linear small-range deformation, incapable of handling nonlinear large-range deformation of biological tissues. It is worth mentioning that the standard Kalman filter is not suitable for being used with NFEM for modelling of nonlinear soft tissue behaviours.

The Extended Kalman filter (EKF) is a typical nonlinear Kalman filtering algorithm. This method is of simple implementation and can track the dynamic behaviours of a nonlinear system via current estimates of state mean and covariance. However, the research on combining EKF with NFEM for real-time soft tissue modelling is still limited. To combine with EKF with nonlinear FEM, the nonlinear FEM model has to be converted into a discrete state-space representation. Given both geometrical and material nonlinearities involved in the nonlinear FEM model, the stiffness function is not constant but depends on displacement, making the formulation of a discrete state-space representation from the nonlinear FEM model into is more complex than that from the linear FEM model [38].

This research work improves our previous work [38] from the linear Kalman filter and FEM for linear small-range deformation to the nonlinear Kalman filter and FEM for nonlinear large-range deformation of soft tissues. It presents an innovative extended Kalman filter nonlinear finite element method (EKF-NFEM) to dynamically predict nonlinear deformation of soft tissues by combination of EKF and NFEM. This method converts the deformation of tissue mechanical into nonlinear filtering to dynamically estimate nonlinear tissue deformation. It discretizes tissue mechanical deformation in the spatial domain via FEM on the basis of nonlinear elastic theory and in the temporal domain via the explicit integration of central difference. Subsequently, the discrete NFEM model is converted into the nonlinear system state models for nonlinear Kalman filtering. Based upon above, a new EKF is established for online estimation of nonlinear mechanical deformation of biological tissues. Haptic feedback in the process of tissue mechanical deformation is also accomplished for surgery simulation. The suggested EKF-NFEM drastically enhances the computational efficiency but without trading off the modelling precision of NFEM. Simulation and experimental analysis along with comparison analysis have been carried out to thoroughly examine the efficacy of the presented EKF-NFEM.

2. Material and Method

2.1. Nonlinear Elasticity

The human tissues belong in the category of hyperelastic materials. The St. Venant–Kirchhoff model represents the most common hyperelastic materials [39]. It involves geometrical and material nonlinearities, where the former reflects the nonlinear relation between displacement-strain relation and the latter the nonlinear relation between stress and strain, both contributing to deformation. It extends the constitutive equations from linear to nonlinear elasticity based on the Lagrangian strain, which is defined by

$$\mathbf{E}=\tfrac{1}{2}(\mathbf{C}-\mathbf{I}) \tag{1}$$

where **C** is the right relative Cauchy–Green strain tensor which is defined as

$$\mathbf{C}=\mathbf{F}^{\mathrm{T}}\mathbf{F} \tag{2}$$

where **F** is the deformation gradient which is expressed by

$$\mathbf{F}=\mathbf{I}+\frac{\partial \boldsymbol{U}}{\partial \mathbf{X}} \tag{3}$$

where $\boldsymbol{U}=[u_x\ u_y\ u_z]$ is the nodal displacement, and $\mathbf{X}=[x,y,z]$ represents the position of a node.

From (2) and (3), (1) can rewritten as

$$\mathbf{E}=\frac{1}{2}\left[\frac{\partial \boldsymbol{U}}{\partial \mathbf{X}}+\frac{\partial \boldsymbol{U}}{\partial \mathbf{X}}^{\mathrm{T}}+\frac{\partial \boldsymbol{U}}{\partial \mathbf{X}}^{\mathrm{T}}\frac{\partial \boldsymbol{U}}{\partial \mathbf{X}}\right] \tag{4}$$

In 4-node tetrahedral elements, the Jacobian matrix of the shape function with respect to nodal coordinates can be defined by

$$[J]\ =\begin{bmatrix}\sum_{I=1}^{N_e}\frac{\partial N_I}{\partial x}u_x & \sum_{I=1}^{N_e}\frac{\partial N_I}{\partial x}u_y & \sum_{I=1}^{N_e}\frac{\partial N_I}{\partial x}u_z\\ \sum_{I=1}^{N_e}\frac{\partial N_I}{\partial y}u_x & \sum_{I=1}^{N_e}\frac{\partial N_I}{\partial y}u_y & \sum_{I=1}^{N_e}\frac{\partial N_I}{\partial y}u_z\\ \sum_{I=1}^{N_e}\frac{\partial N_I}{\partial z}u_x & \sum_{I=1}^{N_e}\frac{\partial N_I}{\partial z}u_y & \sum_{I=1}^{N_e}\frac{\partial N_I}{\partial z}u_z\end{bmatrix} \tag{5}$$

where N_I represents the shape function.

Thus, the Lagrangian strain tensor can be further expressed as

$$\varepsilon_{xx}=\frac{\partial u_x}{\partial x}+\frac{1}{2}\left[\left(\frac{\partial u_x}{\partial x}\frac{\partial u_x}{\partial x}\right)+\left(\frac{\partial u_y}{\partial x}\frac{\partial u_y}{\partial x}\right)+\left(\frac{\partial u_z}{\partial x}\frac{\partial u_z}{\partial x}\right)\right]$$

$$\varepsilon_{yy}=\frac{\partial u_y}{\partial y}+\frac{1}{2}\left[\left(\frac{\partial u_x}{\partial y}\frac{\partial u_x}{\partial y}\right)+\left(\frac{\partial u_y}{\partial y}\frac{\partial u_y}{\partial y}\right)+\left(\frac{\partial u_z}{\partial y}\frac{\partial u_z}{\partial y}\right)\right]$$

$$\varepsilon_{zz} = \frac{\partial u_z}{\partial z} + \frac{1}{2}\left[\left(\frac{\partial u_x}{\partial z}\frac{\partial u_x}{\partial z}\right) + \left(\frac{\partial u_y}{\partial z}\frac{\partial u_y}{\partial z}\right) + \left(\frac{\partial u_z}{\partial z}\frac{\partial u_z}{\partial z}\right)\right]$$

$$2\varepsilon_{xy} = \left(\frac{\partial u_x}{\partial y} + \frac{\partial u_y}{\partial x}\right) + \left[\left(\frac{\partial u_x}{\partial x}\frac{\partial u_x}{\partial y}\right) + \left(\frac{\partial u_y}{\partial x}\frac{\partial u_y}{\partial y}\right) + \left(\frac{\partial u_z}{\partial x}\frac{\partial u_z}{\partial y}\right)\right] \tag{6}$$

$$2\varepsilon_{yz} = \left(\frac{\partial u_y}{\partial z} + \frac{\partial u_z}{\partial y}\right) + \left[\left(\frac{\partial u_x}{\partial y}\frac{\partial u_x}{\partial z}\right) + \left(\frac{\partial u_y}{\partial y}\frac{\partial u_y}{\partial z}\right) + \left(\frac{\partial u_z}{\partial y}\frac{\partial u_z}{\partial z}\right)\right]$$

$$2\varepsilon_{zx} = \left(\frac{\partial u_z}{\partial x} + \frac{\partial u_x}{\partial z}\right) + \left[\left(\frac{\partial u_x}{\partial z}\frac{\partial u_x}{\partial x}\right) + \left(\frac{\partial u_y}{\partial z}\frac{\partial u_y}{\partial x}\right) + \left(\frac{\partial u_z}{\partial z}\frac{\partial u_z}{\partial x}\right)\right]$$

The strain energy density function for the St. Venant–Kirchhoff model is defined as

$$\mathrm{W}(\mathbf{E}) = \frac{\lambda}{2}(tr(\mathbf{E}))^2 + \mu tr(\mathbf{E}^2) \tag{7}$$

where λ and μ are the Lame constants related to the material properties and are expressed as

$$\lambda = \frac{Ev}{(1+v)(1-2v)} \tag{8}$$

and

$$\mu = \frac{E}{2(1+v)} \tag{9}$$

where E is Young's modulus and v is Poisson's ratio.

By differentiating (7) with respect to **E**, the 2nd Piola–Kirchhoff stress **S** for the St. Venant–Kirchhoff model is obtained as

$$\mathbf{S} = \frac{\partial \mathrm{W}(\mathbf{E})}{\partial \mathbf{E}} = \lambda tr(\mathbf{E})\mathbf{I} + 2\mu\mathbf{E} \tag{10}$$

Subsequently, the nonlinear stiffness matrix can be defined as

$$\mathbf{K}(\boldsymbol{U}) = \int_V [\mathbf{B}_N]^{\mathrm{T}}[\mathbf{D}][\mathbf{B}_N] + [\mathbf{B}_G]^{\mathrm{T}}[\boldsymbol{\Sigma}][\mathbf{B}_G]\, dV \tag{11}$$

where $\mathbf{B}_N$ represented for the nonlinear strain-displacement matrix which contains the deformation gradient, $\mathbf{B}_G$ is the linear strain displacement matrix, $\mathbf{D}$ represented for the material matrix, and $\boldsymbol{\Sigma}$ represented for the matrix that contains the 2nd Piola–Kirchhoff stress **S** [39].

2.2. Dynamic Equilibrium System

Applying the governing equation for the motion of the material points of a continuum [34] to each element, the dynamic deformation behaviours of biological tissues can be described as

$$\boldsymbol{M}\ddot{\boldsymbol{U}} + \boldsymbol{C}\dot{\boldsymbol{U}} + \boldsymbol{K}(\boldsymbol{U})\boldsymbol{U} = \boldsymbol{f} \tag{12}$$

where $\dot{\boldsymbol{U}}$ and $\ddot{\boldsymbol{U}}$ are the first- and second-order derivatives of $\boldsymbol{U}$, which represent the nodal velocity and acceleration; the mass matrix $\boldsymbol{M}$ is related to material density; the damping matrix $\boldsymbol{C}$ is determined by $\boldsymbol{C}=\alpha\boldsymbol{M}+\beta\,\boldsymbol{K}(\boldsymbol{U})$ where α and β are the damping coefficients [34]; $\boldsymbol{K}(\boldsymbol{U})$ represents the nonlinear stiffness function which depends on the deformation displacement due to both geometrical and material nonlinearities involved in the nonlinear St. Venant–Kirchhoff material model; and $\boldsymbol{f}$ represents the exerted mechanical force.

The dynamic system (12) can be discretized by either explicit integration or implicit integration. The difference between the explicit and implicit integrations is that the implicit integration directly calculates the displacement, while the explicit integration indirectly calculates the displacement from the acceleration which has to be determined at first. The implicit time integration scheme is stable for large time steps under linear acceleration. However, it has to either solve a system of linear equations or compute the stiffness matrix inversion at each time step, causing a heavy computing cost. In contrast, the explicit time integration is efficient in computation and simple in implementation. In this paper, given its higher accuracy than the explicit Euler integration but still at a small computational cost, the explicit central difference scheme [40] is adopted to resolve unknown displacements at each iteration.

With the explicit central difference scheme, the acceleration and velocity can be described by

$$\begin{aligned}\ddot{\boldsymbol{U}}_t &= \frac{1}{\Delta t}\left(\frac{\boldsymbol{U}_{t+\Delta t} - \boldsymbol{U}_t}{\Delta t} - \frac{\boldsymbol{U}_t - \boldsymbol{U}_{t-\Delta t}}{\Delta t}\right) \\ &= \frac{1}{\Delta t^2}(\boldsymbol{U}_{t-\Delta t} - 2\boldsymbol{U}_t + \boldsymbol{U}_{t+\Delta t})\end{aligned} \tag{13}$$

$$\dot{\boldsymbol{U}}_t = \frac{1}{2\Delta t}(\boldsymbol{U}_{t+\Delta t} - \boldsymbol{U}_{t-\Delta t}) \tag{14}$$

Substituting (13) and (14) into (12) and making simple arrangements yield

$$(\frac{1}{\Delta t^2}\boldsymbol{M}+\frac{1}{2\Delta t}\boldsymbol{C})\boldsymbol{U}_{t+\Delta t} = \boldsymbol{f_t} - (\boldsymbol{K}(\boldsymbol{U}_t)\boldsymbol{U}_t - \frac{2}{\Delta t^2}\ \boldsymbol{M})\ \boldsymbol{U}_t\ -\ (\frac{1}{\Delta t^2}\boldsymbol{M} - \frac{\mathbf{1}}{\mathbf{2\Delta t}}\boldsymbol{C})\boldsymbol{U}_{t-\Delta t} \tag{15}$$

Since the central difference method is conditionally stable, its time step Δt is defined by

$$\Delta t \le \Delta t_{cr} = \frac{L_e}{c} \tag{16}$$

where L_e denotes the smallest characteristic element length and c the speed of a dilatational wave.

2.3. Extended Kalman Filter Nonlinear Finite Element Method

2.3.1. State Space Model

Denote

$$\boldsymbol{R}_t = \boldsymbol{K}(\boldsymbol{U}_t)\boldsymbol{U}_t \tag{17}$$

Apparently, $\boldsymbol{R}_t$ is a nonlinear function of displacement $\boldsymbol{U}_t$, which represents the internal nodal reaction force.

Then (15) can be rewritten as

$$(\frac{1}{\Delta t^2}\boldsymbol{M}+\frac{1}{2\Delta t}\boldsymbol{C})\boldsymbol{U}_{t+\Delta t} = \boldsymbol{f}_t - \boldsymbol{R}_t + \frac{2}{\Delta t^2}\ \boldsymbol{M}\boldsymbol{U}_t\ -\ (\frac{1}{\Delta t^2}\boldsymbol{M} - \frac{\mathbf{1}}{\mathbf{2\Delta t}}\boldsymbol{C})\boldsymbol{U}_{t-\Delta t} \tag{18}$$

By neglecting the damping matrix $\boldsymbol{C}$ due to the small values of the damping coefficients for soft tissues [40], (18) can be rewritten as

$$\frac{1}{\Delta t^2}\boldsymbol{M}\ \boldsymbol{U}_{t+\Delta t} = \boldsymbol{F}_t - \boldsymbol{R}_t + \frac{2}{\Delta t^2}\ \boldsymbol{M}\boldsymbol{U}_t\ -\ \frac{1}{\Delta t^2}\boldsymbol{M}\boldsymbol{U}_{t-\Delta t} \tag{19}$$

Rewrite (19) into state space form

$$\boldsymbol{U}_{t+\Delta t} = \left(2\boldsymbol{U}_t - \boldsymbol{R}_t\frac{\Delta t^2}{\boldsymbol{M}}\right) + \left(\boldsymbol{F}_t\frac{\Delta t^2}{\boldsymbol{M}} - \boldsymbol{U}_{t-\Delta t}\right) \tag{20}$$

Equation (20) can be further expressed as

$$\boldsymbol{U}_{t+\Delta t} = \boldsymbol{A}(\boldsymbol{U}_t) + \boldsymbol{W}_t \tag{21}$$

where

$$\boldsymbol{A}(\boldsymbol{U}_t) = \left(2\boldsymbol{U}_t - \boldsymbol{R}_t \frac{\Delta t^2}{\boldsymbol{M}}\right) \tag{22}$$

$$\boldsymbol{W}_t = \left(\boldsymbol{F}_t \frac{\Delta t^2}{\boldsymbol{M}} - \boldsymbol{U}_{t-\Delta t}\right) \tag{23}$$

2.3.2 Extended Kalman Filter

Consider soft tissue deformation as a dynamic system. According to the state space model given by (21), the system state equation is described as

$$\boldsymbol{U}_{t+\Delta t} = \boldsymbol{z}(\boldsymbol{U}_t, \boldsymbol{W}_t, \boldsymbol{w}_{t+\Delta t}) = \boldsymbol{A}(\boldsymbol{U}_t) + \boldsymbol{W}_t + \boldsymbol{w}_{t+\Delta t} \tag{24}$$

where $\boldsymbol{U}_t$ is the system state vector (the nodal displacement) at time t, $\boldsymbol{W}_t$ is the control input at time t, $\boldsymbol{A}$ represents the system function transformed from time t to $t + \Delta t$, and $\boldsymbol{w}_{t+\Delta t}$ is the process noise, which is supposed as a zero-mean white Gaussian noise with covariance matrix $\boldsymbol{Q}^{\boldsymbol{p}}$.

The system measurement equation is defined as

$$\boldsymbol{y}_{t+\Delta t} = \boldsymbol{H}(\boldsymbol{U}_{t+\Delta t}, \boldsymbol{n}_{t+\Delta t}) \tag{25}$$

where $\boldsymbol{y}_{t+\Delta t}$ denotes the measurement vector, $\boldsymbol{H}$ denotes the measurement function which is represented as an identity matrix, and $\boldsymbol{n}_{t+\Delta t}$ denotes the measurement noise which is supposed as a zero-mean Gaussian white noise with covariance matrix $\boldsymbol{Q}^{\boldsymbol{m}}$. $\boldsymbol{w}_{t+\Delta t}$ and $\boldsymbol{n}_{t+\Delta t}$ are assumed to be uncorrelated.

The filtering process of EKF includes two stages. One is the state prediction described as

$$\overline{\boldsymbol{U}}_{t+\Delta t} = \boldsymbol{A}(\boldsymbol{U}_t) + \boldsymbol{W}_t \tag{26}$$

$$\overline{\boldsymbol{P}}_{t+\Delta t} = \boldsymbol{A}_{\boldsymbol{t}+\Delta \boldsymbol{t}} \boldsymbol{P}_t \boldsymbol{A}_{t+\Delta t}^{\mathrm{T}} + \boldsymbol{Q}^{\boldsymbol{p}} \tag{27}$$

where $\overline{\boldsymbol{U}}_{t+\Delta t}$ and $\overline{\boldsymbol{P}}_{t+\Delta t}$ are the priori estimated displacement and error covariance at time $t + \Delta t$, and $\boldsymbol{A}_{\boldsymbol{t}+\Delta \boldsymbol{t}}$ is the Jacobian matrix of function $\boldsymbol{f}$ in terms of $\boldsymbol{U}_t$, which can be obtained as

$$\boldsymbol{A}_{t+\Delta t} = \frac{\partial \boldsymbol{z}}{\partial \boldsymbol{U}_t}(\boldsymbol{U}_t, \boldsymbol{W}_t, \boldsymbol{w}_{t+\Delta t}) \tag{28}$$

The other is the measurement update which is calculated by

$$\boldsymbol{U}_{t+\Delta t} = \overline{\boldsymbol{U}}_{t+\Delta t} + \boldsymbol{K}_{t+\Delta t}(\boldsymbol{y}_{t+\Delta t} - \boldsymbol{H}\overline{\boldsymbol{U}}_{t+\Delta t}) \tag{29}$$

$$\boldsymbol{P}_{t+\Delta t} = \overline{\boldsymbol{P}}_{t+\Delta t} - \boldsymbol{K}_{t+\Delta t}\boldsymbol{H}\overline{\boldsymbol{P}}_{t+\Delta t} \tag{30}$$

where $\boldsymbol{U}_{t+\Delta t}$ and $\boldsymbol{P}_{t+\Delta t}$ are the posteriori estimated displacement and its error covariance at time $t + \Delta t$.

The Kalman gain is defined as

$$\boldsymbol{K}_{t+\Delta t} = \overline{\boldsymbol{P}}_{t+\Delta t}\boldsymbol{H}^{\mathrm{T}}(\boldsymbol{H}\overline{\boldsymbol{P}}_{t+\Delta t}\boldsymbol{H}^{\mathrm{T}} + \boldsymbol{Q}^{\boldsymbol{m}})^{-1} \tag{31}$$

Since the use of the explicit central difference integration enables the deformation calculations to be conducted at node level [40], there is no need to calculate and assembly the global stiffness matrix at each iteration. Define $\boldsymbol{R}_t$ as

$$\boldsymbol{R}_t = \sum \boldsymbol{R}_t^e \tag{32}$$

where $\boldsymbol{R}_t^e$ is the reaction force for element *e*, which is calculated from the 2nd Piola–Kirchhoff stress **S** and deformation gradient **F** as follows

$$\boldsymbol{R}_t^e = \int_v {}_0^t\mathbf{B}_L^{\mathrm{T}}\, {}_0^t\mathbf{S} d^0V \tag{33}$$

and

$${}_0^t\mathbf{B}_L^{(a)} = \mathbf{B}_{L0}^{(a)}\, {}_0^t\mathbf{F}^{\mathrm{T}} \tag{34}$$

where ${}_0^t\mathbf{B}_L^{(a)}$ is the *a-th* sub-matrix of strain-displacement matrix ${}_0^t\mathbf{B}_L^{\mathrm{T}}$ with *a* indicating the nodal number in each element; ${}_0^t\mathbf{F}^{\mathrm{T}}$ represents the deformation gradient from the initial time to the current time *t*; and $\mathbf{B}_{L0}^{(a)}$ denotes the shape function derivatives in terms of nodal coordinates at the initial stage, and it can be pre-calculated at element level.

As shown in Fig. 1, the EKF-NFEM algorithm involves the following steps:

(i) Set the initial nodal displacements as $\boldsymbol{U}_0 = 0$ and $\boldsymbol{U}_{-\Delta t} = 0$.

For each iteration

{

(ii) For each element

- Calculate ${}^{t}_{0}\mathbf{B}_L^{\mathrm{T}^e}$ and ${}^{t}_{0}\mathbf{S}^e$ from nodal displacements at the pervious time step.
- Calculate $\mathbf{R}^e_t$ by (33) and (34);

(iii) Calculate the global nodal reaction force $\mathbf{R}_t$ by (32).

(iv) For each node

- Conduct state prediction

$$\begin{aligned}\overline{\boldsymbol{U}}^i_{t+\Delta t} &= \boldsymbol{A}(\boldsymbol{U}_t)^i + \boldsymbol{W}^i_t \\ &= \left(2\boldsymbol{U}^i_t - \boldsymbol{R}^i_t\frac{\Delta t^2}{\boldsymbol{M}^i}\right) + \left(\boldsymbol{F}^i_t\frac{\Delta t^2}{\boldsymbol{M}^i} - \boldsymbol{U}^i_{t-\Delta t}\right)\end{aligned} \tag{35}$$

$$\overline{\boldsymbol{P}}^i_{t+\Delta t} = \boldsymbol{A}^i_{t+\Delta t}\boldsymbol{P}^i_t\boldsymbol{A}^{T\,i}_{t+\Delta t} + \boldsymbol{Q}^{\boldsymbol{p}\,i} \tag{36}$$

$$\boldsymbol{K}^i_{t+\Delta t} = \overline{\boldsymbol{P}}^i_{t+\Delta t}\boldsymbol{H}^{\boldsymbol{T}\,i}\left(\boldsymbol{H}^{\,i}\overline{\boldsymbol{P}}^i_{t+\Delta t}\boldsymbol{H}^{\boldsymbol{T}i} + \boldsymbol{Q}^{\boldsymbol{m}\,i}\right)^{-1} \tag{37}$$

- Conduct measurement update

$$\boldsymbol{U}^i_{t+\Delta t} = \overline{\boldsymbol{U}}^i_{t+\Delta t} + \boldsymbol{K}^i_{t+\Delta t}\left(\boldsymbol{y}^i_{t+\Delta t} - \boldsymbol{H}^{\,i}\left(\overline{\boldsymbol{U}}^i_{t+\Delta t}, \boldsymbol{n}^i_{t+\Delta t}\right)\right) \tag{38}$$

$$\boldsymbol{P}^i_{t+\Delta t} = \overline{\boldsymbol{P}}^i_{t+\Delta t} - \boldsymbol{K}^i_{t+\Delta t}\boldsymbol{H}^{\,i}\overline{\boldsymbol{P}}^i_{t+\Delta t} \tag{39}$$

where *i* indicates the *i*th row entry of a matrix.

- Calculate $\boldsymbol{R}_{t+\Delta t}$ from $\boldsymbol{U}_{t+\Delta t}$.

}

It can be seen that the above steps do not involve matrix computation, and thus the computational cost is significantly reduced.

3. Performance Evaluation and Discussion

Simulation and experimental analyses were performed to examine the effectiveness of the suggested EKF-NFEM in terms of soft tissue modelling. For comparison purpose, tests were also conducted under the same conditions by the traditional NFEM, and the resultant displacements were chosen as the reference values to calculate estimation error. Further, haptic feedback for interactive tissue deformation by the proposed EKF-NFEM was also examined.

3.1. Cubic-shape Virtual Tissue Model

Simulations were conducted on a cubic-shape virtual tissue model (see Fig. 2(a)). This cubic-shape tissue model was in the size of $100mm$×$100mm$×$100mm$. It was meshed uniformly into 3760 tetrahedrons with 839 nodes. The mass density of $1000kg/m^3$, Young's module of $30kPa$ and Possion ratio of 0.49, which represent human liver's mechanical attributes [41], were applied to the virtual cubic-shape tissue. A compression trial was performed on the virtual cubic-shape tissue with its bottom face constrained, where a linear compressive force of (0, 0.5*N)* was horizontally applied

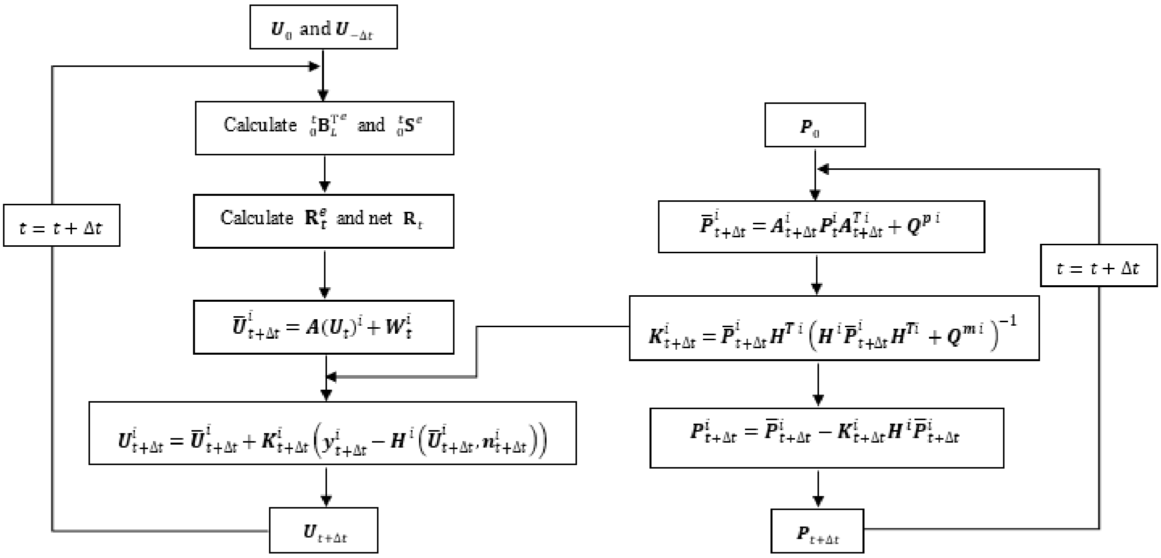

Figure 1. EKF-NFEM algorithm, where U_0 and $U_{-\Delta t}$ represent the initial displacements, and P_0 the initial error covariance.

to the cube's left face (see Fig. 2(a)). The initial state and error covariance were 0 and 0.001. The intensity of the process noise covariance was 0.1. The time step was 0.001*s*.

To have a thorough analysis on the EKF-NFEM performance, two free nodes (i.e., inspection nodes A and B in Fig. 2(a)) in the cubic-shape tissue model were randomly chosen to track their displacements in the deformation process. Inspection node A was located at the center of the cube's left face with the exerted force, where the measurements were obtained by embedding a random Gaussian white noise (Covariance intensity = 0.001 in this case) in the reference values (see Fig. 2(d)). Inspection node B was located at the cube's top face center without the exerted force.

Figs. 2(b) and (c) illustrate the deformations generated by both NFEM and EKF-NFEM for the mechanical test of compression on the cubic-shape tissue model, which are nearly same. To further study the difference, Figs. 2(e) and (f) show the displacements at the two inspection nodes (i.e., inspection nodes A and B). It can be seen that the noise involved in the measurement data (see Fig. 2(d)) is removed, and the displacements at both inspection nodes by EKF-NFEM closely approximate those by NFEM, respectively. Table 1 lists the statistical errors of EKF-NFEM, where the mean absolute error (MAE), root mean square error (RMSE) and standard deviation (SD) at inspection node A are 0.013177*mm*, 0.021447*mm* and 0.016978*mm*, and at inspection node B are 0.011962*mm*, 0.023033*mm* and 0.019749*mm*. Thus, it is clear that the proposed EKF-NFEM has similar accuracy as the traditional NFEM.

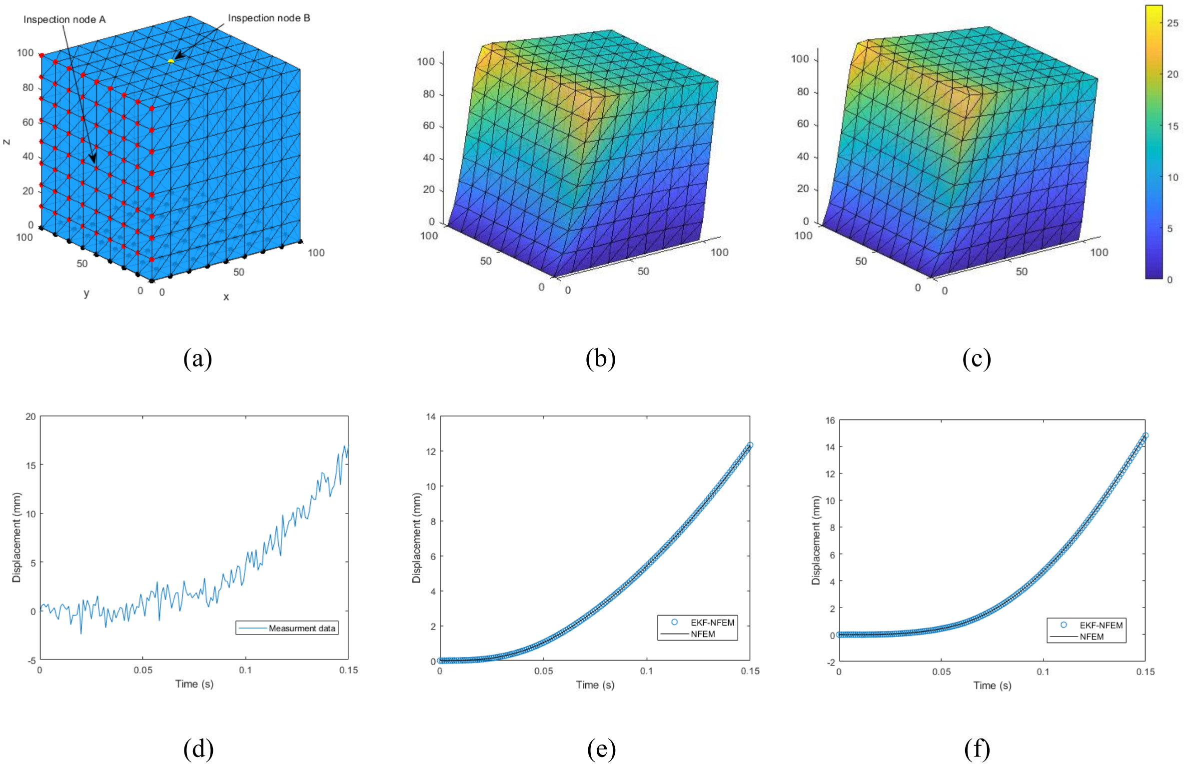

(a) (b) (c)

(d) (e) (f)

Figure 2. Compression test on a virtual tissue model of cubic shape: (a) The undeformed cubic-shape model with two inspection nodes, where all nodes of the bottom face (highlighted in black) were constrained, and a linear compressive force (0, 0.5 *N*) was exerted horizontally to the nodes on the left face (highlighted in red). In addition to inspection node A with the exerted linear compressive force, one free node (inspection node B) in the cube model was also randomly chosen to analyze the deformations of NFEM and EKF-NFEM; (b) NFEM deformation; (c) EKF-NFEM deformation; (d) Measurements of displacement obtained at inspection node A; (e) Displacements at inspection node A; and (f) Displacements at inspection node B.

TABLE 1. MAEs, RMSEs and SDs at both inspection nodes for the simulation case with the cubic-shape model

Inspection node	MAE (mm)	RMSE (mm)	SD (mm)
A	0.013177	0.021447	0.016978
B	0.011962	0.023033	0.019749

3.2. Virtual Human Liver Model

Simulations were performed on a virtual computer model of human liver with 4941 tetrahedrons and 1083 nodes (see Fig. 3(a)). A mechanical test of tensile was carried out on this virtual liver model provided that the nodes (highlighted in black) located on the left side of the top surface were constrained (see Fig. 3(a)). A linear tensile force (0, 0.5*N*) was exerted upwards to the right lobe of the liver, i.e., the nodes highlighted in red on both top and bottom surfaces of the liver (see Fig. 3(a)).

The time step was 0.0001 s. The other simulation parameters were as identical as the simulation case in Section 3.1. In a similar way as the simulation case of Section 3.1, two inspection nodes (inspection nodes A and B) in the computer liver model were chosen for further investigation of the deformations (see Fig. 3(a)). Fig. 3(d) illustrates the measurements obtained at inspection node A.

It can be seen from Figs. 3(b) and (c) that the deformations of both NFEM and EKF-NFEM for the tensile test are nearly same. Figs. 3(e) and (f) further compare the displacements of NFEM and EKF-NFEM at the two inspection nodes, respectively. It is clear that the measurement noise in Fig. 3(d) is removed by EKF-NFEM and the displacements at both inspection nodes by EKF-NFEM closely approximate those by NFEM. Table 2 lists the statistical errors of EKF-NFEM, where the MAE, RMSE and SD at inspection node A are 0.02191mm, 0.03361mm and 0.02554mm, and at inspection node B are 0.02729mm, 0.03419mm and 0.02064mm. Thus, it is obvious that EKF-NFEM is in similar accuracy as NFEM

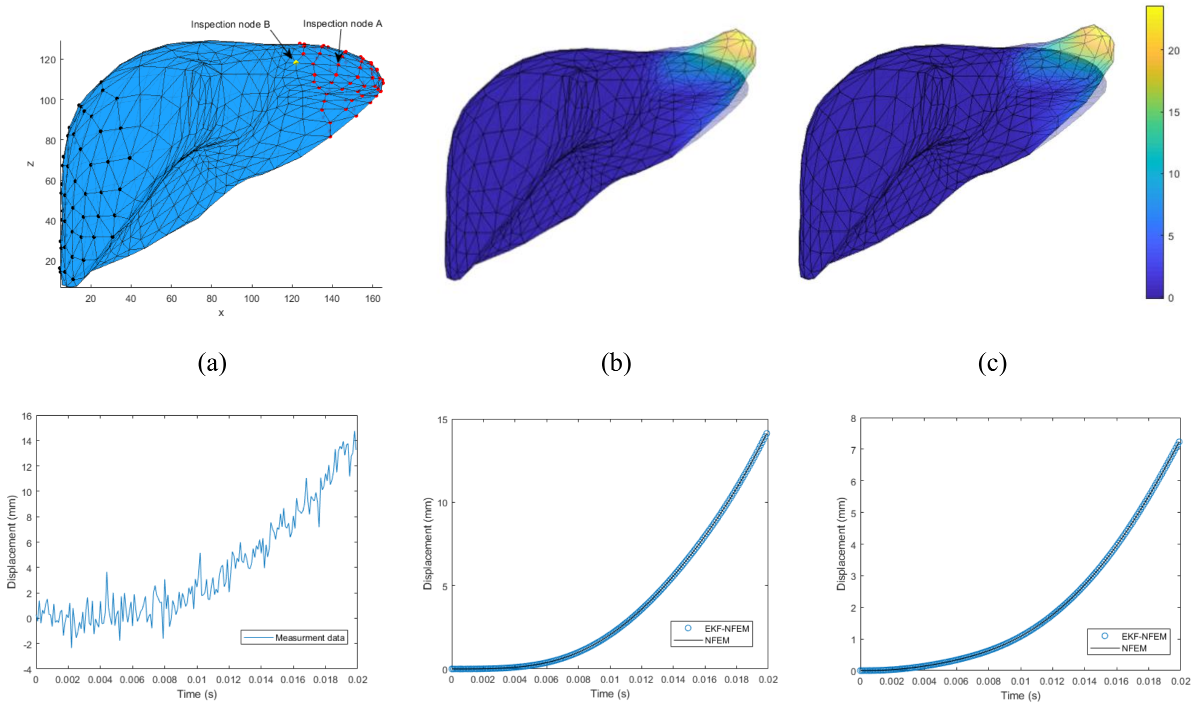

(a) (b) (c)

(d) (e) (f)

Figure 3. Tensile test on a virtual computer model of human liver: (a) The undeformed model, where a linear tensile force (0, 0.5 N) was exerted upwards (in z axis) to the right lobe of the liver (highlighted by the red points), and the nodes (highlighted in black) on the left-top surface were assumed fixed. In addition to inspection node A, a free node (inspection node B) was also randomly chosen in the model to analyze the deformations of NFEM and EKF-FEM; (b) NFEM deformation with reference to the undeformed state (in shading); (c) EKF-NFEM deformation with reference to the undeformed state (in shading); (d) Measurements of displacement obtained at inspection node A; (e) Displacements at inspection node A; and (f) Displacements at inspection node B.

TABLE 2. MAEs, RMSEs and SDs at both inspection nodes for the simulation case with the liver model

Inspection node	**MAE (mm)**	**RMSE (mm)**	**SD (mm)**
A	0.02191	0.03361	0.02554
B	0.02729	0.03419	0.02064

3.3. Computational Performance

The computational efficiencies of both EKF-FEM and NFEM were also studied and compared based on the above simulations, which were realized on a PC with Intel® Core™ i7-8750 2.20GHz CPU, 16.00GB memory and GTX1070 graphics card. The visual fresh rate decreases with the increase of the number of tetrahedral elements, as shown in Fig. 4. For the cubic-shape simulation model of 3760 tetrahedrons in Section 3.1, the visual update rate of NFEM is around 3.5*Hz* which is significantly smaller than the threshold 30*Hz* required by dynamic visual feedback, while the visual update rate of EKF-NFEM is around 75*Hz* which is much higher than the threshold. Similarly, for the liver simulation model of 4941 tetrahedrons in Section 3.2, the visual update rate of NFEM is around 2*Hz*, while that of EKF-NFEM is around 50*Hz* which is much higher than the threshold. Further, EKF-NFEM reaches the threshold 30*Hz* at approximately 8500 tetrahedral elements, while NFEM at approximately 600 tetrahedral elements. Thus, it is clear that in addition to the similar level of accuracy as NFEM, the suggested EKF-NFEM can also achieve the dynamic performance for tissue mechanical deformation.

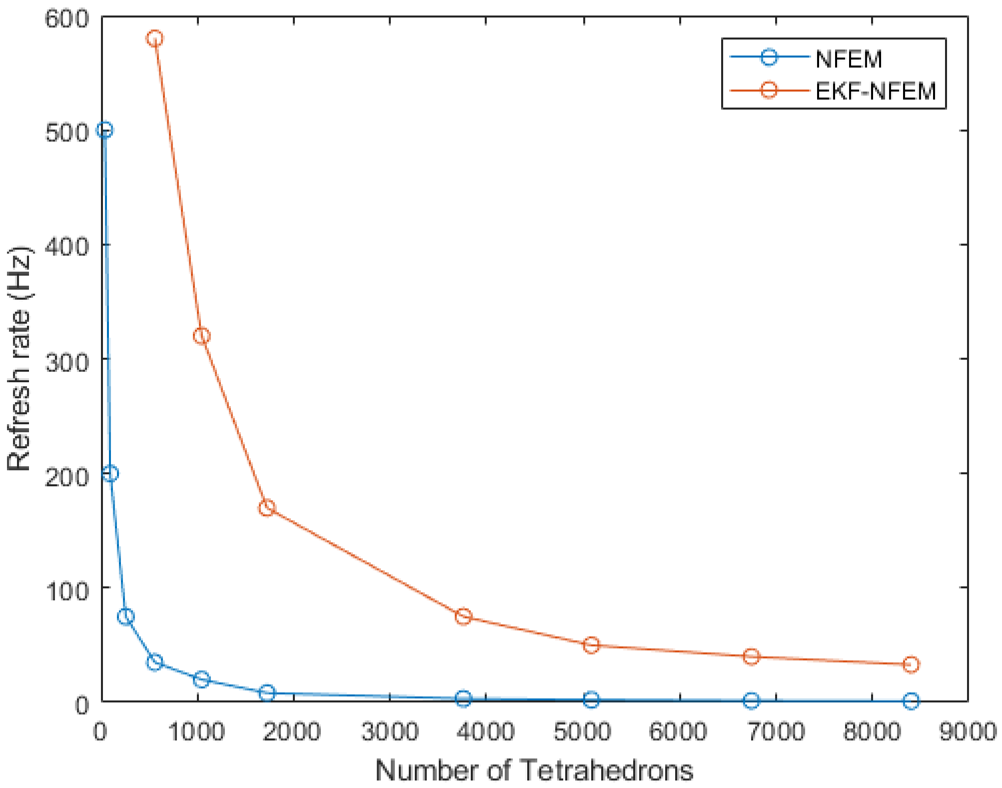

Figure 4. Computational performances of both NFEM and EKF-NFEM.

3.4. Experimental Analysis

Experimental analysis was also performed to examine the effectiveness of the proposed EKF-NFEM for real-time tissue modelling from dynamic measurement of deformation displacement. A mechanical test of compression was performed on a phantom sample of biological deformable tissues using the Instron mechanical testing machine (see Fig. 5(d)). This phantom tissue was made up from Ecoflex 0030 silicone gel (the mass density = 1060kg/m^3, are Shear modulus = 22.081kPa and Possion ratio = 0.5), which has the similar material properties as human tissues [42, 43]. It was in truncated-cone shape with the bottom diameter of 68 mm, the height of 28 mm and the top diameter of 58 mm. It was anchored on a flat and rigid surface and compressed by the Instron machine vertically with a linear force of (0, 0.15 N) exerted at the sample's top face.

For comparison purpose, both NFEM and EKF-NFEM modellings were performed in accordance with the experimental conditions. A virtual sample of truncated-cone shape (see Fig. 5(a)) with a uniform mesh of 2349 tetrahedrons and 559 nodes was modelled in the same geometry, material parameters and loading conditions as the physical sample. Similar to the simulation case in Section 3.1, two inspection nodes (inspection nodes A and B) were also chosen in the virtual sample of truncated-cone shape to analyze the deformations. From the measurements acquired at inspection node A, the phantom tissue's deformations were estimated by EKF-NFEM and subsequently set against NFEM deformations. The initial state and its associated error covariance were 0 and 0.001. Figs. 5(b) and (c) show the deformations generated by EKF-NFEM are well in line with those by NFEM. Figs. 5(e) and (f) further compare the displacements at the two inspection nodes by both methods. It is evident that the measurement noise is removed and the estimated displacements by EKF-NFEM closely approximate those by NFEM. Table 3 lists the statistical errors of EKF-NFEM, where the MAE, RMSE and SD at inspection node A are 0.060494mm, 0.086648mm and 0.062242mm, and at inspection node B are 0.007254mm, 0.009434mm and 0.006051mm.

TABLE 3. MAEs, RMSEs and SDs at both inspection nodes by EKF-NFEM for the experimental case

Inspection node	MAE (mm)	RMSE (mm)	SD (mm)
A	0.060494	0.086648	0.062242
B	0.007254	0.009434	0.006051

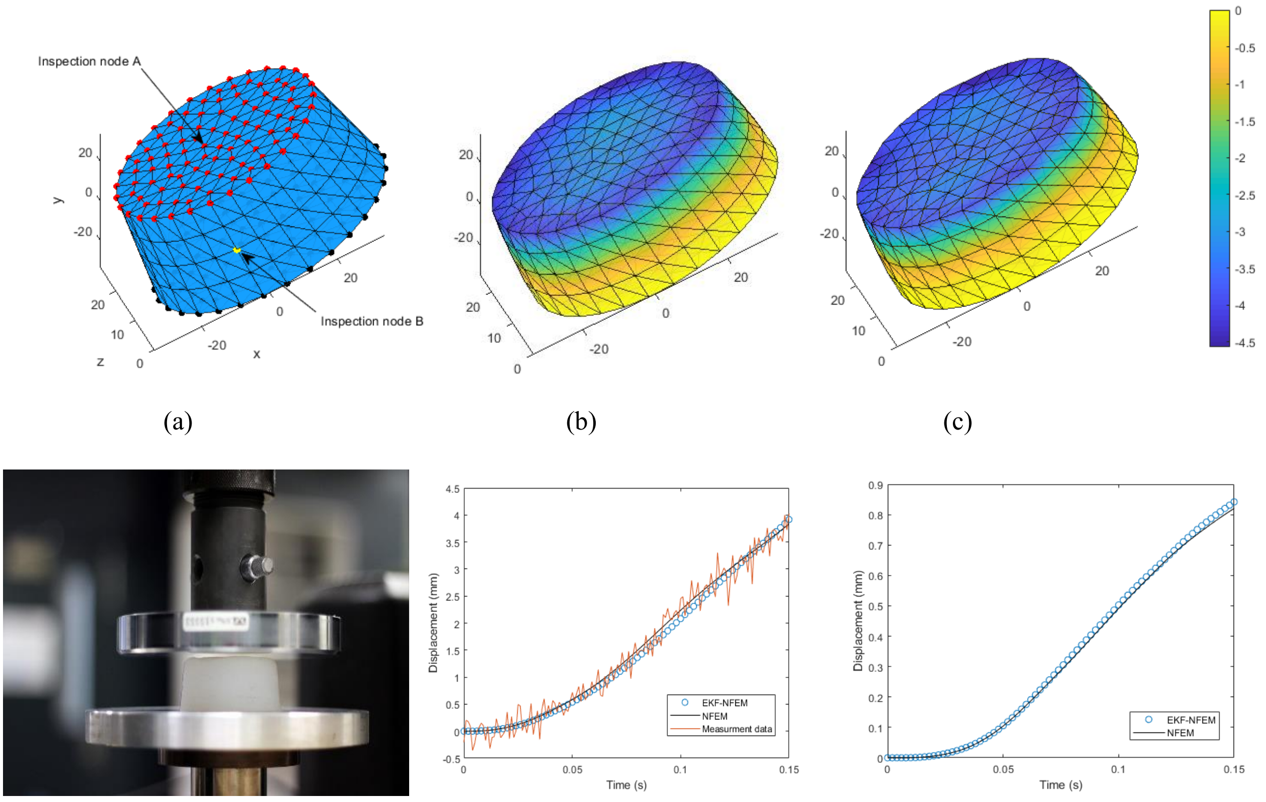

(a) (b) (c)

(d) (e) (f)

Figure 5. Estimation of tissue mechanical deformation from actual measurement: (a) The virtual cylinder-shape tissue model was in the same geometry, material properties and loading and boundary conditions as the phantom tissue sample, where the bottom face (highlighted by the black points) was fixed. In addition to inspection node A at the top face with the exerted force, one more free node (inspection node B) in the virtual tissue model was randomly chosen for comparison of the deformations between NFEM and EKF-NFEM; (b) NFEM deformation; (c) EKF-NFEM deformation; (d) Experimental setup; (e) Displacements at inspection node A; and (f) Displacements at inspection node B.

3.5. Haptic Feedback

Interactive tissue deformation possessing haptic feedback was also achieved by the presented EKF-NFEM via a PHANToM Omni haptic device. The deformation displacement was measured from the penetration depth of the PHANToM endpoint when contacting with the virtual computer model of biological tissues. The reaction force was calculated from (32) and transmitted to the PHANToM system to provide the force feedback. Fig. 6 illustrates the mechanical deformation of a virtual computer model of liver by the virtual haptic needle.

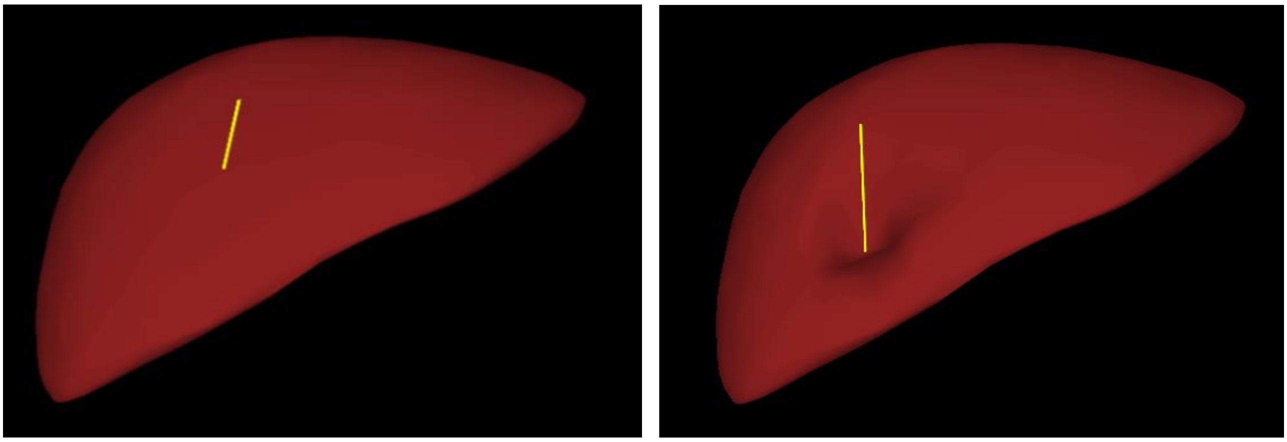

(a) The state before interactive deformation

(b) Interactive deformation state

Figure. 6. Haptic deformation of a computer model of human liver.

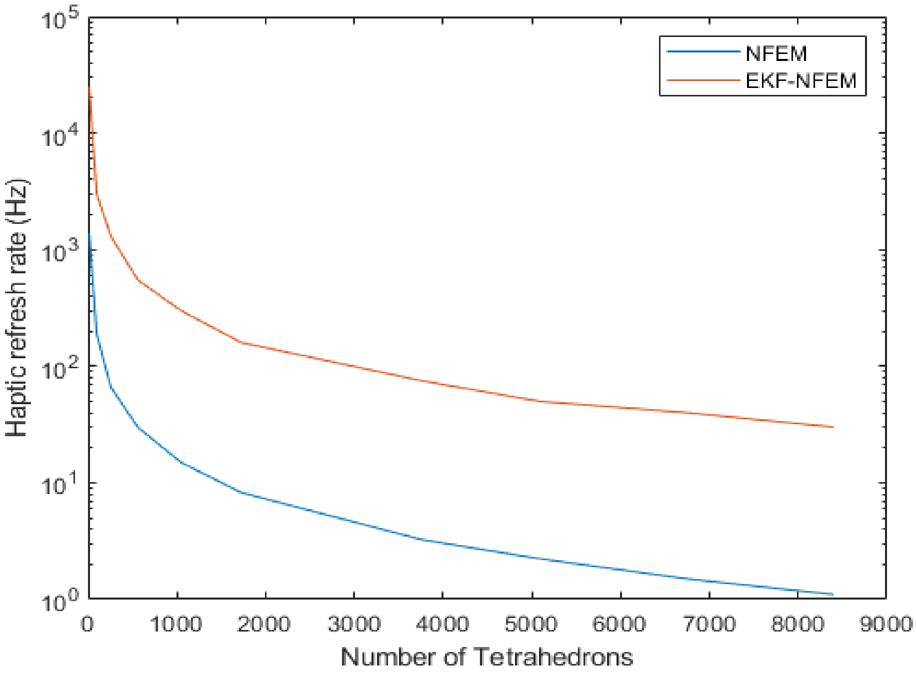

Figure. 7. Haptic performances of both NFEM and EKF-NFEM.

The PHANToM requires the force to be updated at 1,000*Hz* as a minimum for dynamic haptic feedback. As shown in Fig. 7, EKF-NFEM reaches the threshold 1,000*Hz* at approximately 400 tetrahedral elements, but NFEM at approximately 30 tetrahedral elements. Thus, the haptic performance of the presented EKF-NFEM outperforms the traditional NFEM. When the threshold 1,000 Hz cannot be reached, the force extrapolation technique [17] will be used to obtain force information from the previous time step for reliable haptic feedback.

4. Conclusions

This research work presents a new EKF-NFEM for dynamic modelling of nonlinear mechanical deformation of biological tissues. It formulates the soft tissue deformation problem as a nonlinear filtering problem to dynamically estimate tissue mechanical deformation. The contributions of this paper are that the nonlinear state-space equations for filtering estimation are formulated from NFEM to accurately characterize the dynamic behaviours of tissue mechanical deformation and a nonlinear estimation algorithm is further established to dynamically estimate nonlinear deformation of biological tissues. Mechanical deformation of biological tissues is discretized in space via NFEM and in time via the explicit central difference to formulate the state-space equation of the system for Kalman-based nonlinear filtering. On the basis of this, an EKF is developed to online generate posterior statistical estimation of tissue mechanical deformation from dynamic measurement of local displacement. The tissue mechanical deformation possessing haptic feedback is also achieved for surgery simulation. Simulations and experiments together with comparison analysis indicate that the proposed EKF-NFEM drastically enhances the NFEM runtime cost but without the trade-off of the NFEM precision for tissue mechanical deformation.

Future studies will be dedicated to improving the presented EKF-NFEM in two aspects. One is to further improve the computational performance of the proposed EKF-NFEM. At present, the presented EKF-NFEM computes the system equations at node level in serialized, consuming the computational time. However, since the system equations at node level are independent of each other, they can be calculated in parallel. It is expected that advanced parallel computing algorithms will be developed to further improve the computational efficiency of the presented EKF-NFEM. The other is to consider unknown boundary conditions in the estimation of soft tissue deformation. Currently, the proposed EKF-NFEM estimates soft tissue deformation under the assumption that the boundary conditions are known, while the boundary conditions are unknown and variable in actual surgeries. It is expected that advanced algorithms will be developed based on the proposed EKF-NFEM by treating the boundary conditions as additional constraints to constrain the filtering process to achieve online estimation of soft tissue deformation under unknown boundary conditions.

References

[1] H. Delingette, X. Pennec, L. Soler, J. Marescaux, and N. Ayache, "Computational Models for Image-Guided Robot-Assisted and Simulated Medical Interventions," *Proceedings of the IEEE,* vol. 94, pp. 1678-1688, 2006.

[2] K. Miller, "Computational Biomechanics for Patient-Specific Applications," *Annals of biomedical engineering,* vol. 44, p. 1, 2016.

[3] S. A. Cover, N. F. Ezquerra, J. F. O. Brien, R. Rowe, T. Gadacz, and E. Palm, "Interactively deformable models for surgery simulation," *IEEE Computer Graphics and Applications,* vol. 13, no. 6, pp. 68-75, 1993, doi: 10.1109/38.252559.

[4] J. Zhang, Y. Zhong, J. Smith, and C. Gu, "A new ChainMail approach for real-time soft tissue simulation," *Bioengineered,* vol. 7, pp. 246-252, 2016.

[5] J. Zhang, Y. Zhong, and C. Gu, "Ellipsoid bounding region-based ChainMail algorithm for soft tissue deformation in surgical simulation," *International Journal on Interactive Design and Manufacturing (IJIDeM),* vol. 12, pp. 903-918, 2018.

[6] M. Freutel, H. Schmidt, L. Dürselen, A. Ignatius, and F. Galbusera, "Finite element modeling of soft tissues: Material models, tissue interaction and challenges," *Clinical Biomechanics,* vol. 29, pp. 363-372, 2014.

[7] Y. Zou and P. X. Liu, "A high-resolution model for soft tissue deformation based on point primitives," *Computer Methods and Programs in Biomedicine,* vol. 148, pp. 113-121, 2017.

[8] M. Camara, E. Mayer, A. Darzi, and P. Pratt, "Soft tissue deformation for surgical simulation: a position-based dynamics approach," *International Journal of Computer Assisted Radiology and Surgery,* journal article vol. 11, no. 6, pp. 919-928, June 01 2016, doi: 10.1007/s11548-016-1373-8.

[9] J. Bender, D. Koschier, P. Charrier, and D. Weber, "Position-based simulation of continuous materials," *Computers & Graphics,* vol. 44, no. C, pp. 1-10, 2014, doi: 10.1016/j.cag.2014.07.004.

[10] J. Zhang, Y. Zhong, and C. Gu, "Energy balance method for modelling of soft tissue deformation," *Computer-Aided Design,* vol. 93, pp. 15-25, 2017.

[11] Y. Zhong, B. Shirinzadeh, J. Smith, and C. Gu, "Soft tissue deformation with reaction-diffusion process for surgery simulation," *Journal of Visual Languages and Computing,* vol. 23, pp. 1-12, 2011.

[12] J. Zhang, Y. Zhong, J. Smith, and C. Gu, "Neural dynamics-based Poisson propagation for deformable modelling," *Neural Computing and Applications,* vol. 31, pp. 1091-1101, 2019.

[13] J. Zhang, Y. Zhong, and C. Gu, "Deformable Models for Surgical Simulation: A Survey," *IEEE Reviews in Biomedical Engineering,* vol. 11, pp. 143-164, 2018.

[14] J. Zhang, J. Shin, Y. Zhong, D. Oetomo, and C. Gu, "Heat conduction-based methodology for nonlinear soft tissue deformation," *International Journal on Interactive Design and Manufacturing (IJIDeM),* vol. 13, pp. 147-161, 2019.

[15] R. Plantefeve, I. Peterlik, N. Haouchine, and S. Cotin, "Patient-Specific Biomechanical Modeling for Guidance During Minimally-Invasive Hepatic Surgery," *Annals of Biomedical Engineering,* vol. 44, no. 1, pp. 139-153, 2016, doi: 10.1007/s10439-015-1419-z.

[16] J.-M. Schwartz, M. Denninger, D. Rancourt, C. Moisan, and D. Laurendeau, "Modelling liver tissue properties using a non-linear visco-elastic model for surgery simulation," *Medical Image Analysis,* vol. 9, no. 2, pp. 103-112, 2005, doi: 10.1016/j.media.2004.11.002.

[17] J. Zhang, Y. Zhong, and C. Gu, "Neural network modelling of soft tissue deformation for surgical simulation," *Artificial intelligence in medicine,* vol. 97, pp. 61-70, 2019.

[18] W. Wu and P. A. Heng, "An improved scheme of an interactive finite element model for 3D soft-tissue cutting and deformation," *International Journal of Computer Graphics,* vol. 21, no. 8-10, pp. 707-716, 2005, doi: 10.1007/s00371-005-0310-6.

[19] U. Meier, O. López, C. Monserrat, M. C. Juan, and M. Alcañiz, "Real-time deformable models for surgery simulation: a survey," *Computer Methods and Programs in Biomedicine,* vol. 77, pp. 183-197, 2005.

[20] W. Wu and P. A. Heng, "A hybrid condensed finite element model with GPU acceleration for interactive 3D soft tissue cutting," *Computer Animation and Virtual Worlds,* vol. 15, pp. 219-227, 2004.

[21] W. Hou, P. X. Liu, and M. Zheng, "A new model of soft tissue with constraints for interactive surgical simulation," *Computer Methods and Programs in Biomedicine,* vol. 175, pp. 35-43, 2019.

[22] Z. Ullah and C. E. Augarde, "Finite deformation elasto-plastic modelling using an adaptive meshless method," *Computers & Structures,* vol. 118, pp. 39-52, 2013.

[23] Z. A. Taylor, S. Crozier, and S. Ourselin, "A reduced order explicit dynamic finite element algorithm for surgical simulation," *IEEE transactions on medical imaging,* vol. 30, pp. 1713-1721, 2011.

[24] C. Quesada, I. Alfaro, D. González, F. Chinesta, and E. Cueto, "Haptic simulation of tissue tearing during surgery," *International journal for numerical methods in biomedical engineering,* vol. 34, p. e2926, 2018.

[25] N. Lauzeral *et al.*, "A model order reduction approach to create patient-specific mechanical models of human liver in computational medicine applications," *Computer methods and programs in biomedicine,* vol. 170, pp. 95-106, 2019.

[26] F. Martínez-Martínez *et al.*, "A finite element-based machine learning approach for modeling the mechanical behavior of the breast tissues under compression in real-time," *Computers in biology and medicine,* vol. 90, pp. 116-124, 2017.

[27] S. Cotin, H. Delingette, and N. Ayache, "A hybrid elastic model for real-time cutting, deformations, and force feedback for surgery training and simulation," *International Journal of Computer Graphics,* vol. 16, no. 8, pp. 437-452, 2000, doi: 10.1007/PL00007215.

[28] S. A. El-Said, H. M. A. Atta, and A. E. Hassanien, "Interactive soft tissue modelling for virtual reality surgery simulation and planning," *International Journal of Computer Aided Engineering and Technology,* vol. 9, pp. 38-61, 2017.

[29] G. Joldes *et al.*, "Suite of meshless algorithms for accurate computation of soft tissue deformation for surgical simulation," *Medical Image Analysis,* vol. 56, pp. 152-171, 2019.

[30] G. Y. Zhang, A. Wittek, G. R. Joldes, X. Jin, and K. Miller, "A three-dimensional nonlinear meshfree algorithm for simulating mechanical responses of soft tissue," *Engineering Analysis with Boundary Elements,* vol. 42, no. C, pp. 60-66, 2014, doi: 10.1016/j.enganabound.2013.08.014.

[31] A. Wittek, N. Grosland, G. Joldes, V. Magnotta, and K. Miller, "From Finite Element Meshes to Clouds of Points: A Review of Methods for Generation of Computational Biomechanics Models for Patient-Specific Applications," *Annals of Biomedical Engineering,* vol. 44, no. 1, pp. 3-15, 2016, doi: 10.1007/s10439-015-1469-2.

[32] D. Marinkovic and M. Zehn, "Survey of Finite Element Method-Based Real-Time Simulations," *Applied Sciences,* vol. 9, no. 14, p. 2775, 2019.

[33] K. Malukhin and K. Ehmann, "Mathematical Modeling and Virtual Reality Simulation of Surgical Tool Interactions With Soft Tissue: A Review and Prospective," *Journal of Engineering and Science in Medical Diagnostics and Therapy,* vol. 1, p. 020802, 2018.

[34] L. Huafeng and S. Pengcheng, "State-Space Analysis of Cardiac Motion With Biomechanical Constraints," *IEEE Transactions on Image Processing,,* vol. 16, pp. 901-917, 2007.

[35] N. Zeng, Z. Wang, Y. Li, M. Du, and X. Liu, "A hybrid EKF and switching PSO algorithm for joint state and parameter estimation of lateral flow immunoassay models," *IEEE/ACM Transactions on Computational Biology and Bioinformatics,* vol. 9, no. 2, pp. 321-329, 2011.

[36] N. Zeng, Z. Wang, Y. Li, M. Du, and X. Liu, "Inference of nonlinear state-space models for sandwich-type lateral flow immunoassay using extended Kalman filtering," *IEEE Transactions on Biomedical Engineering,* vol. 58, no. 7, pp. 1959-1966, 2011.

[37] N. Zeng, Z. Wang, and H. Zhang, "Inferring nonlinear lateral flow immunoassay state-space models via an unscented Kalman filter," *Science China Information Sciences,* vol. 59, no. 11, p. 112204, 2016.

[38] H. Xie, J. Song, Y. Zhong, and C. Gu, "Kalman Filter Finite Element Method for Real-Time Soft Tissue Modeling," *IEEE Access,* vol. 8, pp. 53471-53483, 2020.

[39] N.-H. Kim, *Introduction to Nonlinear Finite Element Analysis*. Springer US, 2015.

[40] K. Miller, G. Joldes, D. Lance, and A. Wittek, "Total Lagrangian explicit dynamics finite element algorithm for computing soft tissue deformation," *Communications in numerical methods in engineering,* vol. 23, no. 2, pp. 121-134, 2007.

[41] I. Peterlík, C. Duriez, and S. Cotin, "Modeling and Real-Time Simulation of a Vascularized Liver Tissue," *Medical Image Computing and Computer-Assisted Intervention--MICCAI 2012,* pp. 50--57, 2012.

[42] V. Egorov, S. Tsyuryupa, S. Kanilo, M. Kogit, and A. Sarvazyan, "Soft tissue elastometer," *Medical Engineering and Physics*, vol. 30, no. 2, pp. 206-212, 2008, doi: 10.1016/j.medengphy.2007.02.007.

[43] L. J. Sparks *et al.*, "Use of Silicone Materials to Simulate Tissue Biomechanics as Related to Deep Tissue Injury," *Advances in Skin & Wound Care*, vol. 28, pp. 59-68, 2015.